



HAL
open science

Ionospheric detection and localization of volcano eruptions on the example of the April 2015 Calbuco events

Ksenia Shults, Elvira Astafyeva, Sevan Adourian

► **To cite this version:**

Ksenia Shults, Elvira Astafyeva, Sevan Adourian. Ionospheric detection and localization of volcano eruptions on the example of the April 2015 Calbuco events. *Journal of Geophysical Research Space Physics*, 2016, 121 (10), pp.10,303-10,315. 10.1002/2016JA023382 . insu-02139376

HAL Id: insu-02139376

<https://insu.hal.science/insu-02139376>

Submitted on 24 May 2019

HAL is a multi-disciplinary open access archive for the deposit and dissemination of scientific research documents, whether they are published or not. The documents may come from teaching and research institutions in France or abroad, or from public or private research centers.

L'archive ouverte pluridisciplinaire **HAL**, est destinée au dépôt et à la diffusion de documents scientifiques de niveau recherche, publiés ou non, émanant des établissements d'enseignement et de recherche français ou étrangers, des laboratoires publics ou privés.

RESEARCH ARTICLE

10.1002/2016JA023382

Key Points:

- Using GNSS receivers we study ionospheric response to the 22–23 April 2015 Calbuco volcano eruptions
- CVID amplitude is largely defined by eruption intensity and by the background ionospheric conditions
- Using ionospheric measurements, we can not only detect eruptive volcanoes but also determine an eruption onset

Supporting Information:

- Supporting Information S1
- Animation S1
- Animation S2

Correspondence to:

E. Astafyeva,
astafyeva@ipgp.fr

Citation:

Shults, K., E. Astafyeva, and S. Adourian (2016), Ionospheric detection and localization of volcano eruptions on the example of the April 2015 Calbuco events, *J. Geophys. Res. Space Physics*, 121, 10,303–10,315, doi:10.1002/2016JA023382.

Received 28 AUG 2016

Accepted 28 SEP 2016

Accepted article online 30 SEP 2016

Published online 19 OCT 2016

Corrected 7 NOV 2016 and 16 DEC 2016

This article was corrected on 7 NOV 2016 and 16 DEC 2016. See the end of the full text for details.

Ionospheric detection and localization of volcano eruptions on the example of the April 2015 Calbuco events

Ksenia Shults¹, Elvira Astafyeva¹, and Sévan Adourian²

¹Institut de Physique du Globe de Paris, Paris Sorbonne Cité, Univ. Paris Diderot, Paris, France, ²Ecole Normale Supérieure, Paris, France

Abstract Using data from ground-based Global Navigation Satellite Systems (GNSS) receivers located in southern Chile, we study the ionospheric total electron content (TEC) response to two eruptions of the Calbuco volcano that occurred on 22–23 April 2015. In both cases, the TEC response showed quasi-periodic signals with several consecutive wave trains. The averaged amplitude of the observed covolcanic TEC perturbations amounted 0.45 total electron content unit, $1 \text{ TECU} = 10^{16} \text{ el m}^{-2}$ (TECU) for the first eruption and 0.16 TECU for the second one. We compare amplitudes of the TEC response to volcano eruptions of different intensity from our and previously published data, and we show that both the intensity and the background ionospheric conditions define the amplitude of ionospheric covolcanic disturbances. The relative contribution, however, scales with the eruption intensity. The traveltimes diagrams allowed to estimate the propagation speed of the observed covolcanic TEC perturbations as $\sim 900\text{--}1200 \text{ m/s}$, which is close to the acoustic (or shock acoustic) waves speed at the ionospheric height. The spectrograms are consistent with the conclusion on the acoustic nature of the observed TEC perturbations. Finally, we use the approximation of a spherical wave propagating at a constant velocity from a point source, and for the first time, we calculate the location of the volcanic source and the onset time of the volcano eruption from ionospheric measurements. We show that even from 30 s ionospheric GPS data it is possible to “localize” the eruptive source within several degrees of latitude/longitude.

1. Introduction

Ionosphere is the ionized region of the Earth’s upper atmosphere (from 60 to 1000 km), whose state is mainly determined by the solar radiation, and is also largely controlled by the solar and magnetic activities. Besides such influence from above, the ionosphere is also sensible to the influence from below, as earthquakes, propagating tsunamis and erupting volcanoes can generate perturbations in ionospheric parameters [Blanc, 1985]. A part from the detection of coseismic [e.g., Calais and Minster, 1995; Afraimovich et al., 2001, 2010; Liu et al., 2011; Rolland et al., 2011, 2013; Komjathy et al., 2012; Astafyeva et al., 2013a, 2014; Perevalova et al., 2014], cotsunamic [e.g., Liu et al., 2006; Galvan et al., 2012; Kherani et al., 2012; Occhipinti et al., 2013], and covolcanic [e.g., Heki, 2006; Dautermann et al., 2009a, 2009b; Nakashima et al., 2016] ionospheric perturbations, the ionospheric total electron content (TEC) measurements on the example of the December 2004 Sumatra and the March 2011 Tohoku-oki earthquakes have proved to be able to provide information on parameters and localization of a seismic fault ruptured during an earthquake [Heki et al., 2006; Astafyeva et al., 2011, 2013b]. The TEC can be easily measured by dual-frequency receivers of the Global Navigation Satellite System (GNSS) [Hofmann-Wellenhof et al., 2008] that is nowadays widely used for a variety of geodetic applications, allowing rapid estimation of crustal motion/displacements.

The recent development of the GNSS such as American Global Positioning System (GPS), Russian GLONASS (in Russian: GLObal’naya NAVigazionnaya Sputnikovaya Sistema), European Galileo or Chinese BeiDou, along with a good coverage of the ground-based GNSS receivers, makes it possible to ensure the ionospheric detection of all those events. Consequently, nowadays, ionospheric TEC response to earthquakes and tsunamis is sufficiently well investigated and documented [e.g., Calais and Minster, 1998; Afraimovich et al., 2001, 2010, 2013; Heki and Ping, 2005; Liu et al., 2010; Astafyeva et al., 2009, 2013a, 2014; Rolland et al., 2010; Kherani et al., 2012; Occhipinti et al., 2013; Reddy and Seemala, 2015]. Thus, it is now known that the coseismic ionospheric variations often comprise several “modes,” including the ionospheric representation of propagation of the surface Rayleigh wave, of acoustic waves and/or gravity (tsunami) waves. In addition, large

earthquakes are often accompanied by the acoustic resonance signatures [Choosakul *et al.*, 2009; Liu *et al.*, 2011; Rolland *et al.*, 2011].

Contrary to the coseismic and cotsunamic ionospheric perturbations, the variations triggered by the volcano eruptions and/or explosions, which we call here covolcanic ionospheric disturbances (CVIDs), are yet less studied and understood.

Heki [2006] seemed to be the first to use the GPS-TEC measurements to study the ionospheric response to volcano eruptions on the example of the Asama volcano explosion in Japan on 1 September 2004. The explosion itself was rather moderate (vulcanian explosion) and caused a small-amplitude (~ 0.03 – 0.16 total electron content unit, $1 \text{ TECU} = 10^{16} \text{ el m}^{-2}$ (TECU)) TEC response ~ 12 min after the beginning of the explosion. The apparent velocities of the observed TEC perturbations were estimated to be ~ 1.1 km/s, which is close to the speed of the acoustic and shock acoustic waves in the ionosphere. The dense coverage of the Japanese network of GPS receivers (GEONET) allowed detecting the response as far as 200 km away from the volcano. From the GPS-TEC measurements it was also possible to estimate the energy of the Asama volcano explosion as of 2×10^{14} J.

Dautermann et al. [2009a] used data of GPS receivers located around Guadeloupe, Antigua, and the Caribbean to analyze the ionospheric TEC response to the 13 July 2003 explosion of the Soufrière Hill Volcano (SHV) in Montserrat, Lesser Antilles. They observed quasi-periodic TEC oscillations with a period of about 12 min; the TEC response appeared ~ 18 min after the explosion and lasted for about 40 min. Overall, the covolcanic TEC perturbations were registered as far as ~ 700 – 800 km, and their propagation speed was estimated to be ~ 550 – 650 m/s. Spectral analysis revealed peaks centered at 1 and 4 mHz, which is consistent with the theory, suggesting both gravity and acoustic wave components [Kanamori *et al.*, 1994]. *Dautermann et al.* [2009b] used a normal mode summation technique and showed that the 4 mHz peak can be explained by a single explosive source in the atmosphere. *Dautermann et al.* [2009a] estimated the energy of the SHV explosion to be 1.53×10^{10} J.

More recently, *Nakashima et al.* [2016] by using GNSS receivers from the several local networks in Sumatra and Indonesia analyzed the TEC response to the Kelud volcano explosion in February 2014. They reported observations of harmonic oscillations following the 2014 Kelud eruption that were caused by the atmospheric resonance due to the eruption and lasted for ~ 2.5 h.

In this work, we use data from ground-based GNSS receivers to study the ionospheric TEC response to the two April 2015 Calbuco eruptions in southern Chile. We compare our results with previous observations, and we show that the relative amplitude of CVID scales with the intensity of an eruption. Then, we use a simple model of the spherical wave approximation to “localize” the source of the observed ionospheric perturbations. In addition to that, we estimate the onset time of the eruptions.

2. The April 2015 Calbuco Eruptions

On 22 April 2015 the Calbuco volcano, located in southern Chile (41.326°S ; 72.614°W), awoke after 43 years of inactivity. According to seismic data, the first eruption began at 21:04 UT (18:04 LT) on 22 April 2015, preceded by only an hour-long period of volcano-tectonic activity. This first eruption lasted 90 min and generated a sub-Plinian (i.e., medium to large explosive event) and gray ash plume that rose 15 km above the main crater and drifted mainly eastward-northeastward, although fine ash drifted northward and northwestward. A larger second event on 23 April began at 04:00 UT (01:00 LT), it lasted 6 h and also generated a sub-Plinian ash plume that rose higher than 15 km and drifted northward, northeastward, and eastward. The volcanic explosivity index (VEI), which is used to describe the size of an explosive volcanic eruption, was estimated to be 4 for these two events (<http://www.sernageomin.cl> and <http://www.onemi.cl>).

It should be noted that the above mentioned time of the beginning of the eruptions was estimated from the nearest seismic station located at about 100 km away from the volcano. Such a long distance from the volcano source does not allow precise estimation of the volcano eruption time. Besides the seismometer data and in addition to them, it is possible to estimate the time of eruption from infrasound stations [e.g., *Matoza et al.*, 2011; *Caudron et al.*, 2015]. For the above mentioned two Calbuco events, the time was estimated 21:10 UT and 04:00 UT, respectively (A. Le Pichon, private communication, 2016). The error of estimation is about ± 5 min.

Table 1. Information on GNSS Sites Used in the Present Study

Site	Sampling Rate	Data	Network	Latitude	Longitude	Distance
osor	15 s	GPS, GLO	CAP Andes	-40.488	-73.104	102
bche	15 s	GPS, GLO	RAMSAC	-41.039	-71.299	115
nieb	15 s	GPS	CAP Andes	-39.758	-73.401	187
esqu	15 s	GPS, GLO	RAMSAC	-42.815	-71.323	197
mhin	15 s	GPS	CAP Andes	-39.319	-73.215	229
tmco	30s	GPS, GLO	CAP Andes	-38.651	-72.614	297
lnqm	30s	GPS, GLO	CAP Andes	-38.341	-71.362	350
trgn	15 s	GPS	CAP Andes	-38.121	-72.672	357
ango	15 s	GPS, GLO	CAP Andes	-37.680	-72.692	406
pecl	15 s	GPS, GLO	CAP Andes	-37.571	-73.651	428
udec	15 s	GPS, GLO	CAP Andes	-37.356	-72.345	442
laja	15 s	GPS	CAP Andes	-37.269	-71.376	465
antc	30s	GPS, GLO	IGS	-37.222	-71.532	467
ma01	15 s	GPS, GLO	RAMSAC	-38.838	-68.057	477
plvp	15 s	GPS, GLO	CAP Andes	-37.032	-73.585	486
chml	30s	GPS	CAP Andes	-37.243	-70.150	501
nihu	15 s	GPS	CAP Andes	-36.276	-72.397	561
25ma	15 s	GPS, GLO	RAMSAC	-37.656	-67.716	587
cbqc	15 s	GPS	CAP Andes	-36.028	-36.028	590
chim	15 s	GPS, GLO	CAP Andes	-39.051	-66.147	606
cauq	15 s	GPS	CAP Andes	-35.849	-72.341	611
lnrs	30s	GPS	CAP Andes	-35.731	-71.629	629
pane	15 s	GPS	CAP Andes	-35.598	-71.202	650
nrvl	15 s	GPS	CAP Andes	-35.424	-72.095	659
mgue	30s	GPS, GLO	IGS	-35.658	-69.398	691
lhcl	15 s	GPS	RAMSAC	-37.887	-65.595	714
hlne	15 s	GPS	CAP Andes	-34.884	-71.745	722
pmqe	15 s	GPS	CAP Andes	-34.427	-71.630	773
pclm	30s	GPS	CAP Andes	-34.263	-72.004	786
pata	15 s	GPS, GLO	RAMSAC	-40.688	-62.989	812
mzga	15 s	GPS, GLO	RAMSAC	-34.858	-67.696	839
mzsr	15 s	GPS	RAMSAC	-34.494	-68.334	847
rgao	30s	GPS	CAP Andes	-34.124	-69.380	849
sanp	15 s	GPS	CAP Andes	-33.752	-71.481	850
melp	15 s	GPS, GLO	CAP Andes	-33.556	-71.151	875
srlp	15 s	GPS, GLO	RAMSAC	-36.504	-64.280	899
cuvi	15 s	GPS	CAP Andes	-33.231	-71.134	911
mzau	15 s	GPS, GLO	RAMSAC	-33.614	-69.118	913
vbca	15 s	GPS, GLO	RAMSAC	-38.587	-62.269	934
valp	30s	GPS	IGS	-32.904	-71.626	942
mzae	15 s	GPS	RAMSAC	-33.132	-68.150	994
mzac	15 s	GPS, GLO	RAMSAC	-32.772	-68.876	1009
suar	15 s	GPS, GLO	RAMSAC	-37.342	-61.931	1021
sl01	15 s	GPS, GLO	RAMSAC	-33.034	-66.314	1079
gvil	15 s	GPS	RAMSAC	-34.912	-63.014	1102
3aro	15 s	GPS, GLO	RAMSAC	-38.268	-60.274	1108
rufi	15 s	GPS	RAMSAC	-34.141	-62.710	1182
azul	15 s	GPS, GLO	RAMSAC	-36.649	-59.881	1217
peba	15 s	GPS, GLO	RAMSAC	-33.824	-60.562	1350
unro	15 s	GPS, GLO	RAMSAC	-32.837	-60.628	1421
igm1	15 s	GPS, GLO	RAMSAC	-34.451	-58.439	1459
ma02	15 s	GPS, GLO	RAMSAC	-34.486	-58.394	1460
lpgs	30s	GPS, GLO	IGS	-34.786	-57.932	1476

3. Data and Methods Used

To study the ionospheric response to the 2015 Calbuco eruptions, we used data from GNSS stations of the network RAMSAC (Red Argentina de Monitoreo Satelital Continuo), IGS (International GNSS Service), and CAP Andes (Central and Southern Andes GPS Project) within 1500 km of the volcano (Table 1).

Ground-based GNSS observations offer a powerful method for remote sensing of the ionosphere. The space segment of GPS system is composed of 32 satellites in medium Earth orbit on altitude 20,200 km with an inclination of approximately 55°. The GPS signals are transmitted on two distinct carrier frequencies, $f_1 = 1575.42$ MHz and $f_2 = 1227.6$ MHz, and each satellite also broadcasts its own unique pseudorandom noise code which is used to identify the satellite's signal. The dispersive property of the ionosphere provides an opportunity to measure directly the total electron content—electron density integrated along the raypath from the satellite to receiver [Klobuchar, 1985]:

$$\text{TEC} = \int_{\text{raypath}} N(\vec{r}) d\vec{r} \quad (1)$$

The differential (relative) slant TEC (sTEC) is calculated from the linear combination:

$$\text{TEC} = \frac{1}{A} \cdot \frac{f_1^2 f_2^2}{f_1^2 - f_2^2} (L_1 \lambda_1 - L_2 \lambda_2 + \text{const} + nL), \quad (2)$$

where $A = 40.308 \text{ m}^3/\text{s}^2$, $L_1 \lambda_1$ and $L_2 \lambda_2$ are additional paths of the signal caused by the phase delay in the ionosphere, const is unknown initial phase path, caused by the unknown number of total phase rotations along the raypath, and nL are errors in determining the phase path.

Besides the GPS-derived TEC, we also compute TEC using data from GLONASS satellites. The GLONASS constellation consists of 24 satellites that operate in circular orbits at an altitude of 19,100 km, with inclination of 64.8° [Hofmann–Wellenhof et al., 2008, <https://www.glonass-iac.ru/en/>; http://www.navipedia.net/index.php/GLONASS_Space_Segment]. The main difference between GPS and GLONASS is that in GLONASS each satellite has its own frequency but the same code:

$$f_1 = 1602 + k \cdot 0.5625 \text{ MHz}, \quad f_2 = 1246 + k \cdot 0.4375 \text{ MHz}, \quad (3)$$

where k represents the frequency channel which may be known from GLONASS navigation file. Further TEC from GLONASS observables is calculated using the same equation as GPS. The GPS and GLONASS satellites are distinguished by letters G and R, respectively. TEC is measured in TEC units (TECU) that is equal to 10^{16} electrons/ m^2 . It should be noted that the accuracy of the differential TEC estimation from phase measurements is quite good—about 0.01–0.02 TECU [e.g., Afraimovich et al., 2001; Coster et al., 2013].

We apply this method to data from 20 permanent dual-frequency GNSS sites available near the Calbuco volcano at the time of the eruptions. Since the TEC is an integral parameter, the observed ionospheric disturbance accounts for a large range of altitudes. The commonly used mapping function for the ground-based TEC conversion is a thin shell model that assumes ionospheric electron densities occupy a thin spherical shell surrounding the Earth at the height H_{ion} of the peak ionosphere ionization (F_2 layer) [Klobuchar, 1985]. Then sTEC values are associated to an ionospheric pierce point (IPP) latitude and longitude of which is the point of intersection of a line of sight with this thin shell. The propagation of CID is representing by subionospheric points (SIPs) that are the projections of the IPPs at the Earth's surface. In this paper we assumed H_{ion} at 270 km of altitude for the first eruption and 400 km for the second one. We take H_{ion} above the maximum height of the ionospheric F_2 region, as can be seen in lines #1 and #2 of Table 2. To remove multipath effect on low elevation angles we used the cutoff elevation mask of 10°.

Seven GPS and eight GLONASS satellites were visible at the time of the first Calbuco eruption and of eight GPS and six GLONASS satellites—at the time of the second eruption. However, most significant TEC perturbations were observed only in data of satellites G01, G03, G17, G23, G32, and R07 on 22 April and G13, G28, and R13 on 23 April. During the eruptions, these satellites mainly sounded the area on the north from the volcano (Figure 1a). Figure 1b shows the relative unfiltered TEC time series derived at site ANGO for GPS satellites G01, G03, and G32 and GLONASS satellite R07 on 22 April 2015 from 20:30 UT to 23:30 UT. TEC perturbations with multiple oscillatory pulses can be clearly seen between 21:20 and 23:00 UT. An example of the TEC response to the second Calbuco eruption is shown in Figure 1c. One can see that the perturbation occurs in the TEC data series ~1 h after the beginning of the eruption at 4 UT.

To further analyze the TEC response to the both Calbuco eruptions, we used fourth-order Butterworth zero-phase band-pass filter that allows extract variations in the range 3–10 mHz.

Table 2. Main Characteristics of the TEC Response (From GNSS Measurements) and the Background Ionospheric Conditions (From the Online IRI Model) During the Eruptions of the Calbuco Volcano in April 2015 and During Other Historical Eruptions Studied by Using the Ionospheric GPS/GNSS Measurements^a

Date	Name	Location (Lat; Lon)	UT	LT	VEI	<A>, TECU	TEC, TECU	dTEC, %	H _m F ₂ , km	V, m/s	Reference	
#1	22/4/2015	Calbuco	-41.32; -72.61	21:04	18:04	4	0.45	29.3	15	249	~930	Current paper
#2	23/4/2015	Calbuco	-41.32; -72.61	04:00	01:00	4	0.16	10.8	18	346	~1200	Current paper
#3	13/2/2014	Kelud	-7.93; 112.31	15:50	22:50	4	~0.4	25.1	16	326	~800	Nakashima et al. [2016]
#4	01/9/2004	Asama	36.4; 138.52	11:02	20:02	2	0.1	11.9	8	300	1100	Heki, [2006]
#5	13/7/2003	Soufrière Hill	16.71; -62.18	03:35	23:35	3	0.15	13.7	11	326	~700	Dautermann et al. [2009a, 2009b]

^aThe relative TEC contribution (dTEC, %) is calculated from the average amplitude of TEC response divided by the background TEC value.

Animations S1 and S2 in the supporting information show TEC perturbations following the first and the second Calbuco volcano eruptions, respectively, as seen by all GNSS receivers mentioned in Table 1, and by all visible GPS and GLONASS satellites. In response to the first eruption, the amplitude of TEC variations first increased 15 min after the beginning of the eruption (Animation S1). The second wave train was then clearly seen at ~21:45 UT. At ~22:45 UT the third wave train occurred. All the perturbations were prominent on the north-northeast from the volcano. Also, we see propagation of the perturbation in the north-northeast direction.

After the second eruption, intensive quasi-periodic TEC fluctuations started to occur at ~4:50 UT on the north-northeast from the volcano; the perturbations lasted for about 30–40 min (Animation S2). The amplitude of these TEC variations was smaller than during the first eruption. We discuss this difference in detail below.

Figures 2a and 2c show filtered TEC series from 20:30 UT to 23:00 UT on 22 April 2015 as measured by the GNSS receivers around the volcano by satellites G03 and G23, respectively. One can notice the occurrence of quasi-periodic oscillations in the TEC about 15 min after the beginning of the eruption at 21:04 UT at the nearest SIPs. This is in agreement with the theoretical propagation time of an acoustic perturbation from the ground to ionosphere altitude. At the majority of stations, the TEC response registered by G03 and G23 contained three wave chains, the second occurred ~23 min after the first one, the third one with ~63 min delay (Figures 2a and 2c). The second wave packet had remarkably larger amplitude than the first

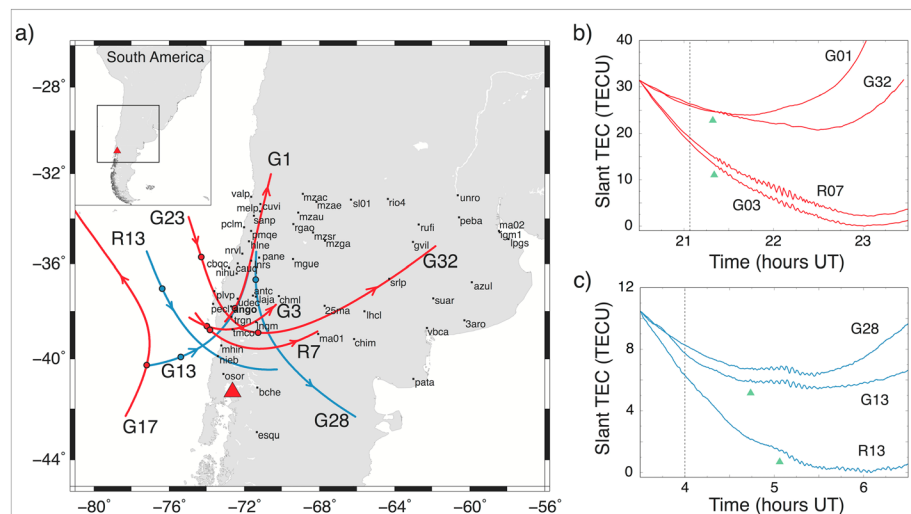


Figure 1. (a) Map of the southern South America showing the location of Calbuco volcano (red triangle) and the GNSS sites used in this study (small black dots). Red curves show the trajectories of subionospheric points (SIPs) as seen by GNSS receiver ANGO for GPS G01, G03, G32, and GLONASS R07 satellites during 20–24 UT on 22 April 2015 (i.e., before, during, and after the first eruption). Blue curves show the SIP tracks for GPS G13, G28, and GLONASS R13 satellites during 03–07 UT on 23 April 2015 (i.e., before, during, and after the second eruption). The name of the ANGO receiver is marked in bold black letters. The satellite labels are shown in large black letters next to the SIP curves. Black outlined circles on the tracks indicate SIPs at the eruption time for both events; (b, c) Slant TEC time series recorded by ANGO station and the above mentioned satellites during the eruptions on 22 and 23 April 2015, respectively. The “seismological” time of the eruptions is indicated by dashed vertical line. The red triangles indicate the onset of covolcanic perturbations.

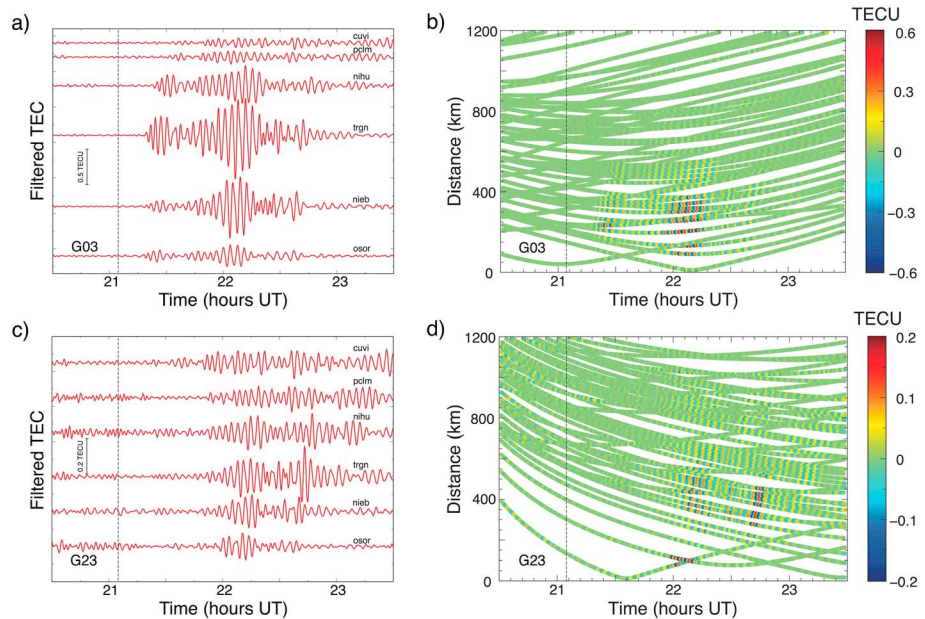


Figure 2. TEC response to the first Calbuco eruption on 22 April 2015. The 3–10 MHz band-pass filtered slant TEC series for (a) G03 satellite and for (c) G23 satellite. The names of GNSS-stations are written above each TEC curve; (b, d) the corresponding traveltime diagrams. Dashed lines indicate the time of the eruption. Color shows the TEC amplitude, and the corresponding color scale is shown on the right.

and third ones. The wave chains lasted for about 1.7 h as observed by G03. At larger distances from Calbuco, the arrival times increased showing spatial propagation of the perturbation. The propagation of perturbations as well as their correlation with the Calbuco volcano position can be clearly seen from the traveltime diagram shown in Figures 2b and 2d. We estimate the propagation speed to be ~976 m/s for the first wave train, ~897 m/s for the second one, and ~935 m/s for the third one. From these values of propagation speed, we attribute these modes to acoustic ones, which usually propagate at the typical sound speed 0.8–1 km/s at the ionospheric heights.

The filtered TEC variations following the second eruption, as well as the corresponding traveltime diagrams, are shown in Figure 3. One can see that the TEC response to the second eruption is also quasi-periodically shaped, which is in line with previous observations of ionospheric response to volcano eruptions. However, contrary to the first eruption, the TEC response was registered only ~50–60 min after the beginning of the eruption. Also, the second eruption mostly provoked one to two wave trains, as compared to three wave trains in the first case. The amplitude of the TEC response reached its maximum at ~1 h after the beginning of the eruption.

The traveltime diagrams plotted for the TEC variations following the second eruption show the apparent propagation speeds of ~1300 m/s and ~1100 m/s for the first and the second wave trains, respectively, which is higher than during the first eruption but yet is in agreement with previous observations [e.g., Heki, 2006].

The traveltime diagrams in Figures 2 and 3 show that in both cases the covolcanic TEC perturbations were visible as far as 600–700 km away from the volcano. This might indicate on the acoustic nature of the observed TEC perturbations, as it is known that this component does not usually propagate far from the source [e.g., Astafyeva et al., 2009]. As compared to coseismic ionospheric disturbances, CVID have smaller amplitudes and do not propagate as far as the coseismic perturbations.

Further comparison of Figures 2 and 3 shows that the first eruption generated TEC perturbations of larger amplitude than the second one. It should be pointed out that the amplitude of ionospheric perturbations is significantly influenced by the magnetic field [Calais and Minster, 1995; Afraimovich et al., 2001; Heki and Ping, 2005; Rolland et al., 2013]. The plasma perturbations cannot propagate perpendicularly to the magnetic field lines; therefore, the poleward propagation is impeded, while the equatorward propagation is favored. In addition to that, at midlatitudes the angle between the ionospheric perturbation propagation direction and the magnetic field line plays a role: a perturbations propagating at angles larger than $\pm 10^\circ$ with magnetic

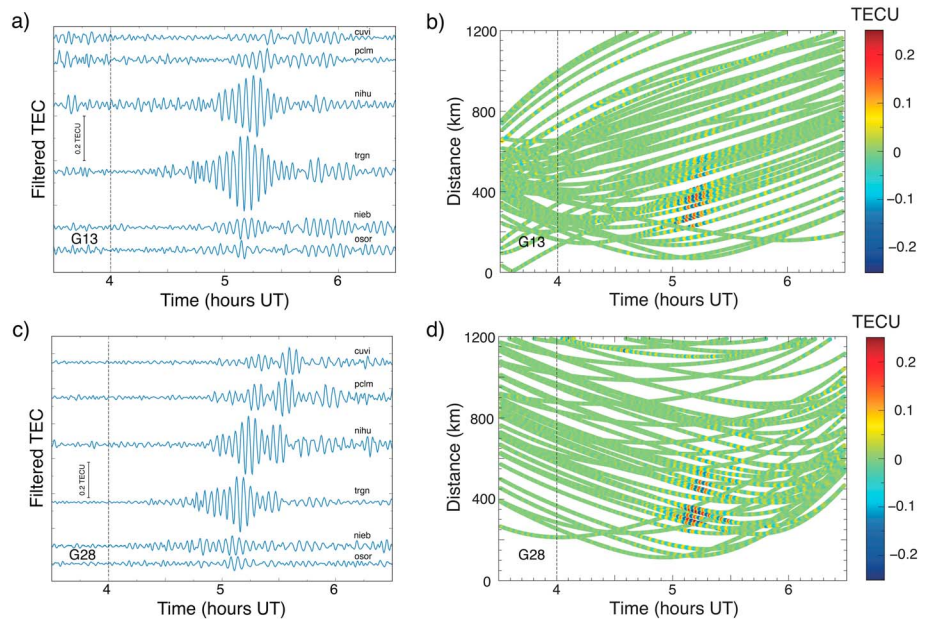


Figure 3. The same as Figure 2 but for the second eruption of the Calbuco volcano on 23 April 2015. The satellites are (a, b) G13 and (c, d) G28.

field lines would be attenuated by a factor of 0.5 [Rolland *et al.*, 2013]. This attenuation factor is 0.25 for angles larger than $\pm 30^\circ$, and for ionospheric perturbations propagating at $\sim \pm 45^\circ$ to magnetic field lines the amplitude is close to 0. Therefore, in order to correctly compare the amplitudes of the TEC response to the two Calbuco eruptions, we take into account the above criteria and count only CVID propagating at small angles to magnetic field lines. At the location of the Calbuco volcano the inclination of the magnetic field is 8.2° (<http://www.ngdc.noaa.gov/geomag-web/>). From the near-field TEC observations on the north-northeast from the volcano, we estimate the mean amplitude of the TEC response to be 0.45 TECU for the first eruption and 0.16 TECU for the second eruption.

It is surprising to observe such a huge difference in amplitudes between the two Calbuco eruptions. As mentioned earlier, both eruptions were classified as VEI 4 events, whereas seismological stations (<http://www.sernageomin.cl> and <http://www.onemi.cl>) and infrasound stations (R. Matoza, private communication, 2015) showed that the second eruption was stronger than the first one.

It was shown previously for earthquakes of different magnitudes that the amplitude of ionospheric TEC response increases with the magnitude of an earthquake [Astafyeva *et al.*, 2013a, 2014; Cahyadi and Heki, 2015]. Therefore, in similar manner, we would expect the ionospheric response to the second Calbuco eruption to be of larger amplitude than that to the first eruption. However, it is not the case as we see in our results. This could be explained by the fact that during the second eruption the background ionospheric TEC value was almost 3 times smaller as compared to the time of the first eruption, as shown in Table 2. The first eruption occurred during local evening time, while the second during local nighttime. It is known that the ionospheric parameters have strong diurnal variations. Therefore, despite the two eruptions were separated in time by only 7 h, the background ionospheric parameters changed significantly. Consequently, after the second eruption, the waves propagating from below entered in the medium with poorer ionization and generated ionospheric perturbations with smaller amplitude.

To further study the amplitude dependence on the eruption intensity, we involve into our analysis previous results on observations of CVID by using the GNSS technique. The main characteristics of the TEC response to the three recent volcano eruptions and the background ionospheric conditions during the time of their ionospheric detection are presented in Table 2. We estimated the averaged TEC response from the results presented in the works cited in Table 2, and we calculated the background TEC level by using the online IRI-2007 model [Bilitza *et al.*, 2011] (http://omniweb.gsfc.nasa.gov/vitmo/iri_vitmo.html) for the time and location of the eruptions. Data in Table 2 demonstrate that the TEC amplitude is larger for the detection of CVID

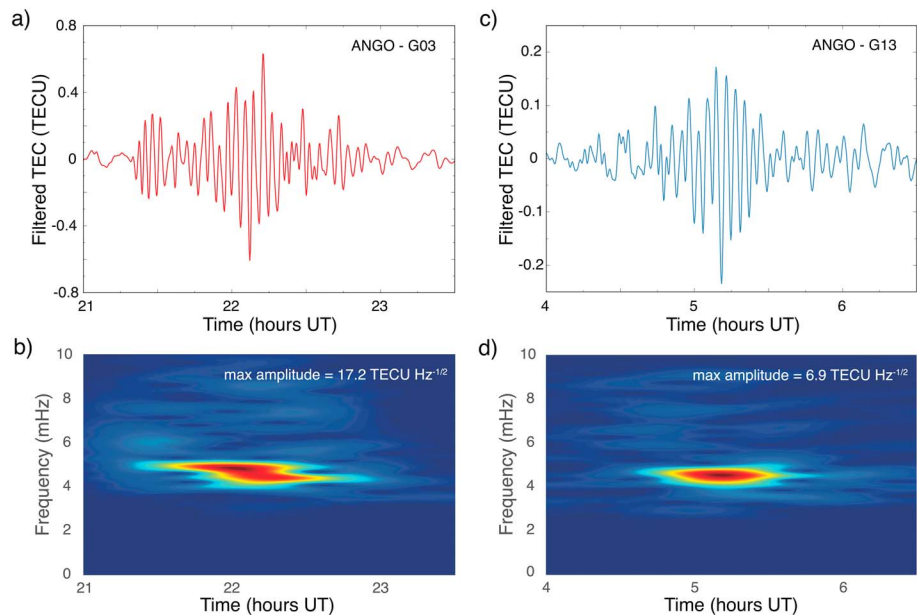


Figure 4. Spectrograms computed by using a Hamming window width of 75 min and 74 overlap between consecutive windows for (a, c) station ANGO and satellite G03 for the first eruption and (b, d) station ANGO and satellite G13 for the second eruption.

on the background of denser ionization and, consequently, higher absolute TEC values. Therefore, we conclude that both the intensity of the eruption and the background ionospheric TEC value define the amplitude of the perturbation. The relative $d\text{TEC}/\text{TEC}$ contribution varies from 8 to 18%. The strongest perturbation contribution to the background absolute TEC is observed for the most intensive eruptions, which is similar to earthquake cases [Astafyeva *et al.*, 2013a, 2014; Cahyadi and Heki, 2015].

We computed the spectrogram associated with TEC time series as observed by ANGO station for G03 satellite using a Hamming window width of 75 min and 74 overlap between consecutive windows (Figures 4a and 4c). The spectrogram clearly shows the energy peaks between ~ 3.8 and ~ 5.2 mHz, which corresponds to the period between the first and third harmonic of the atmospheric trapped acoustic modes [e.g., Watada and Kanamori, 2010]. These results are in agreement with conclusions made earlier from traveltime diagrams (Figures 2 and 3) on the acoustic nature of the observed perturbations and are in line with previous observations of the TEC response to volcano eruptions [Dautermann *et al.*, 2009a; Nakashima *et al.*, 2016].

For the second Calbuco eruption, the spectrogram also shows the peaks within the acoustic modes frequencies (Figures 4b and 4d), which is also in line with previous observations and with our conclusions.

4. Localization of the Volcano Eruption From the Ionosphere. Estimation of the Time of Eruption

The method of the ionospheric “localization” of a perturbation source was first proposed by Afraimovich *et al.* [2006] for the ionospheric detection of a source of seismic origin, i.e., of an earthquake epicenter. This method was successfully tested for the detection of the seismic source of several large earthquakes that occurred in Japan and in Sumatra in 1994–2006 [Afraimovich *et al.*, 2006; Kiryushkin and Afraimovich, 2007; Astafyeva *et al.*, 2009; Kiryushkin *et al.*, 2011]. In this work, we use similar method to estimate the location and the onset time of the two eruptions of the Calbuco volcano on 22–23 April 2015. It should be noted that in the case of CVID, the waveform of the TEC perturbations is more complex than that of coseismic ionospheric perturbations. The latter are commonly reported to be characterized by an N wave shape, so that the minimum and maximum of the TEC variations can be determined easily. Consequently, the perturbation appears easier to “track.” In the case of covolcanic variations, the TEC response is most often quasi-periodically shaped; therefore, it is more difficult to determine precisely the “tracking” parameters such as the minimum and maximum of the TEC response. This is the first application of the proposed method to detection of a volcanic source.

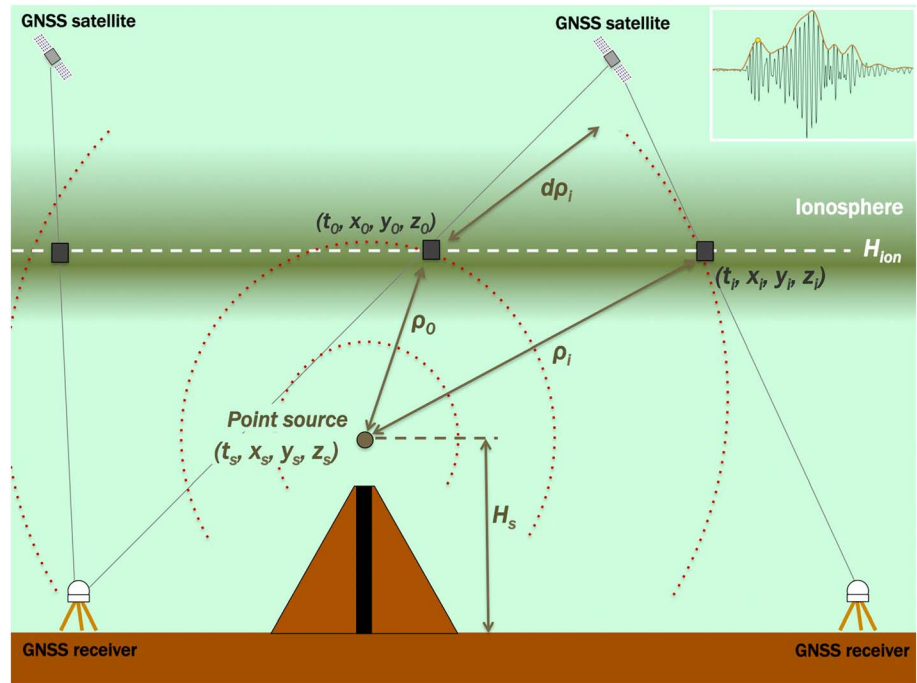


Figure 5. A scheme of the spherical wave approximation used to localize the “secondary” point source (x_s, y_s, z_s) located at the height H_s . Time t_s is the onset time of the secondary source. We assume that the covolcanic perturbation propagates in the form of a spherical wave at the constant velocity V from the point source to detection points (x_i, y_i, z_i) located at the altitude H_{ion} , which is the altitude of the thin shell ionosphere as taken for the GNSS sounding. The reference point (x_0, y_0, z_0) is the point of the first detection of the perturbation at time t_0 ; ρ_0 is the distance traveled by the wave from the point source up to reference point; ρ_i is the distance between ρ_i and ρ_0 . Small panel in the upper right corner shows an example of covolcanic TEC variations. Small yellow point shows the “tracking” point of the CVID, that is further used as a point of CVID detection.

In the framework on this approximation, the point source can be located in the atmosphere but not only on the ground. The conception of such “secondary” source comes from the theory of vertical propagation of acoustic waves from the ground, where they dissipate at the altitude of more than ~ 110 km [Blanc, 1985]. The dissipation heats the medium, and this heated area serves as a sort of secondary source of atmospheric/ionospheric disturbances.

To detect the source location from ionospheric TEC measurements, we first determine the TEC maximum from the waveform envelope (as shown in Figure 5, panel in the upper right corner). Second, we assume that the perturbation propagates from a point source with coordinates (x_s, y_s, z_s) located at an altitude H_s , as a spherical wave with constant velocity V (Figure 5). The perturbation first arrives at the reference point (x_0, y_0, z_0) at time t_0 , and it is further detected at farther located points (x_i, y_i, z_i) at times t_i . The altitude of all ionospheric detection points is H_{ion} which is the height of the ionospheric thin shell assumed for the GNSS sounding. In the case of the Calbuco eruptions, the H_{ion} was 270 km for the first eruption and 400 km for the second eruption.

We further solve a system of equations for a distance traveled by the spherical wave from the point source to the reference point (ρ_0) and to the i th point (ρ_i), and we compute the time delay of the perturbation arrival in registration points. The distance traveled by the perturbation between the reference point and the i th point is determined as $d\rho_i = \rho_i - \rho_0$, as shown in Figure 5. We make these calculations for all possible values of the point source coordinates and the height H_s , as well as CVID propagation speed V . For each combination of parameters, we compute an error between the spherical wave model and the real observations, and the result with the minimal value of the error corresponds to the final solution. Finally, the onset time of the source at altitude H_s is calculated from the computed parameters-propagation velocity V , the coordinates of the source (x_s, y_s, z_s) , and the arrival time t_0 of the disturbance in the reference point:

$$t_s = t_0 - \frac{\sqrt{(x_0 - x_s)^2 + (y_0 - y_s)^2 + (z_0 - z_s)^2}}{V} \tag{4}$$

Table 3. Results of Computation of the Source of Ionospheric Disturbances Generated During the April 2015 Calbuco Eruptions^a

Site-Sat. Used	Lat. (°N)	Long. (°E)	Time (UT, h)	H _s (km)	V _r (m/s)
<i>Event of 22 April 2015 (Day 112)</i>					
ango-G03, chml-G03, plvp-G03	-43.4	-72.7	21.1773	140	500
ango-G03, tmco-G03, chml-G03	-40.6	-73.2	21.3952	140	850
ango-G03, chml-G03, laja-G03, pecl-G03	-40.8	-72.5	21.3237	140	500
25ma-G17, laja-G03, pecl-G03	-42.0	-72.2	21.2239	140	440
25ma-G17, lnrs-G03, cbqc-G03	-41.8	-73.1	21.2441	140	460
25ma-G17, pane-G03, nrvl-G03	-41.0	-73.6	21.2801	140	460
25ma-G17, chml-G03, laja-G03, pecl-G03	-41.2	-72.4	21.2658	140	420
chim-G17, tmco-G03, mhin-G03	-40.2	-73.8	21.3850	140	640
plvp-G03, chml-G03, laja-G03	-41.3	-72.6	21.2870	140	480
nihu-G03, cauc-G03, lnrs-G03	-41.2	-73.5	21.1936	140	360
25ma-G17, lhcl-G17, chml-G03	-40.4	-72.7	21.3056	140	420
<i>Event of 23 April 2015 (Day 113)</i>					
ango-G13, chml-G13, plvp-G13	-43.5	-70.2	4.94337	300	400
ango-G13, tmco-G13, chml-G13	-39.8	-71.3	5.14292	300	1190
ango-G13, chml-G13, laja-G13, pecl-G13	-39.1	-71.5	5.12943	300	720
25ma-R13, laja-G13, pecl-G13	-39.8	-71.9	4.98877	300	300
25ma-R13, pane-G13, nrvl-G13	-39.1	-71.6	5.05413	300	400
25ma-R13, chml-G13, laja-G13, pecl-G13	-39.3	-71.5	5.11475	300	640
plvp-G13, chml-G13, laja-G13	-38.8	-71.3	5.10822	300	460
nihu-G13, cauc-G13, lnrs-G13	-38.6	-71.4	5.06638	300	340
25ma-R13, antc-G13, plvp-G13	-38.1	-69.6	5.14142	300	850
ma01-R13, pecl-G13, trgn-G13	-43.0	-70.6	5.04570	300	940
ma01-R13, laja-G13, chml-G13	-42.2	-72.5	5.04021	300	890

^aThe Calbuco volcano coordinates are (-41.326 N; -72.614E).

The results of the application of the localization method for detection of both eruptions are presented in Table 3 and also in Figure 6. One can see that for the first eruption the coordinates of the source of the ionospheric perturbation can be localized sufficiently well even from 3 to 4 ionospheric detection points by using our algorithm. The position of the source is estimated within ±1–2° of latitude and longitude. The radial velocity of the perturbation varies from 360 to 850 m/s for different “groups” of ionospheric points, while the height of the source is 140 km in all cases. The time of the source onset at 140 km varies from ~21.18 to ~21.39 UT. Considering the traveling time of the acoustic waves from the ground (or volcano top) to the height of 140 km, which is about 0.1 h, we then estimate the eruption time 21.07 to 21.29 UT, which is close to the onset time estimated from seismometers (21.07 UT) and from the infrasound stations (21.0 UT ± 0.12 h).

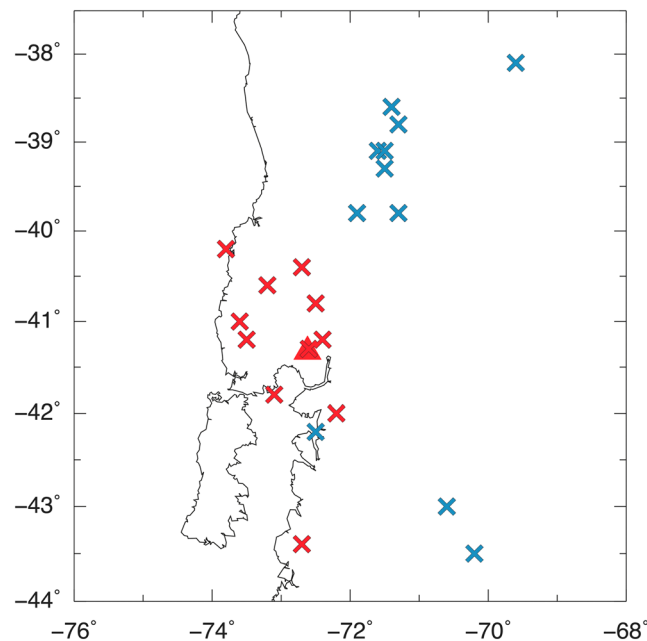


Figure 6. Map showing positions of the Calbuco volcano (red triangle) and positions of the secondary source as estimated from ionospheric measurements (crosses). Red crosses correspond to the first eruption and blue crosses to the second.

Similarly, we apply the method to the results of the CVID registered after the second eruption. We find that the source can be localized from the ionospheric TEC measurements within

several degrees of latitude and longitude (Table 3 and Figure 6). Depending on the position of the ionospheric detectors, the radial velocity of the detected CVID varies from 400 to 1190 m/s. The height of the secondary source was found to be 300 km in all cases, which is 160 km higher than for the first case. The latter is, most likely, related to the difference in the actual profiles in the ionospheric electron density and in 100 km difference in the maximum height of the ionospheric F_2 layer (H_mF_2), as shown in Table 2. In addition, such difference in the secondary source height can also be partly due to the fact that during the second eruption the volcanic ash plume rose higher than during the first one, so that the erupted mass was pushed higher into the atmosphere and “raised” the height of the secondary source.

The estimated time of the secondary source onset varies from ~4.94 to ~5.14 UT. Considering the propagation time of acoustic waves from the ground until the secondary source height of 300 km (~600 s), we estimate the eruption time to be 4.78 to 4.98 UT. We note that in this case the ionospherically estimated eruption time is much delayed as compared to the onset time estimated from the seismometers and from the infrasound stations. Such time delay occurs because of the late occurrence and registration of the CVID after the second eruption – 50–60 min, as compared to 15 min in the first eruption case, as mentioned above.

One can notice that for both eruptions the secondary source is located on the northeast from the volcano. From Table 3 and Figure 6 it follows that this “displacement” is stronger for the second eruption. Such effect might be due to significant impact of horizontal atmospheric winds on vertical propagation of CVID. Also, it is interesting to note that our results are in line with the drift direction of the volcanic plume following the two eruptions, as mentioned in section 2. Therefore, our estimations are in agreement with the real volcanic observations.

5. Discussions and Conclusions

The sudden ejection of material during an explosive eruption generates a broad spectrum of pressure oscillations, including both acoustic and gravity waves [Kanamori *et al.*, 1994]. Partly, these waves further propagate in the atmosphere and ionosphere and can be detected by atmospheric and ionospheric sounding instruments. Acoustic waves can also be trapped in the lower atmosphere and further leak into the ionosphere, demonstrating ionospheric signatures of acoustic resonant oscillations [Dautermann *et al.*, 2009a; Nakashima *et al.*, 2016]. As a result, depending on the “source” below, the covolcanic signatures in the ionospheric TEC could have different waveforms: N wave is usually known to occur in response to a volcano Plinian explosion [Heki, 2006], while acoustic resonance and gravity waves usually generate quasi-periodic TEC oscillations [Dautermann *et al.*, 2009a, 2009b; Nakashima *et al.*, 2016]. In our work, we found quasi-periodic signal following the two eruptions of 22–23 April 2015, and from traveltime diagrams and from spectrograms we attribute the observed TEC signatures to acoustic nature and related to the acoustic resonance.

Concerning the intensity of volcano eruptions and the corresponding TEC response, we know on the example of the Asama volcano that ionospheric response can be detected to eruptions with VEI more than 2 [Heki, 2006]. Although the Asama volcano explosion produced TEC variations of sufficiently small amplitude (maximum ~0.1 TECU), the ionospheric response was detectable by the dense network of GPS receivers in Japan. The comparative analysis reveals that volcano eruptions with VEI 3 and more generate ionospheric perturbations with larger amplitudes. In this work we have shown that the background ionospheric TEC plays an important role in the formation of the amplitude of a CVID. However, the relative contribution of the CVID to the background TEC value is larger for more intensive volcano eruption. This result is similar to the scaling law of coseismic ionospheric disturbances generated by earthquakes of different magnitudes.

The propagation speeds of CVID can vary from ~550–650 m/s [Dautermann *et al.*, 2009a, 2009b] to 1.3 km/s and can reveal either gravity or acoustic components. Slower velocities are usually attributed to gravity waves, whereas faster perturbations are generally provoked by acoustic modes, or shock acoustic waves in the case of velocities exceeding the sound speed.

It should be noted that nowadays “simple” observation of ionospheric response to natural hazard events like earthquakes, tsunami propagation, or volcano eruptions become systematic and already less surprising. The next step in the development of the modern geophysics is in use of the ionospheric measurements for

seismological and/or volcanological applications. For instance, *Astafyeva et al.* [2011, 2013b] used high-resolution 1 Hz ionospheric TEC data from ground-based GPS receivers and obtained the first ionospheric images of the seismic fault ruptured during the 2011 Tohoku-oki earthquake. In addition, *Astafyeva et al.* [2013b] showed that multisegment structure of seismic fault can be seen from the ionosphere. More recently, *Reddy and Seemala* [2015] studied ionospheric response to the 2015 Gorkha earthquake and found that the asymmetry in the radial distribution of the ionospheric coseismic perturbation propagation speed corresponded to the upper crustal heterogeneity.

In terms of ionospheric detection of the source, *Afraimovich et al.* [2006] seemed to be the first who applied the results of observations of ionospheric TEC response to earthquakes for localization of an earthquake's epicenter. By using an approximation of a spherical wave propagating at constant velocity, they managed to estimate the position of the seismic source for the December 2004 Sumatra earthquake and for the September 2003 Hokkaido earthquake. Later, *Liu et al.* [2010] used a different method to localize the epicenter of the Chi-Chi earthquake from ionospheric TEC response. Their method was based on the ray-tracing and the beam-forming techniques.

In the current work, for the first time, we detected the position of an eruptive volcano from points of registration of CVID, i.e., from the ionosphere. In addition to that, we were able to estimate the time of the beginning of the Calbuco eruptions that occurred on 22–23 April 2015. For the first eruption, the results seem quite promising for both the source coordinates and the eruption time; however, for the second eruption the accuracy was much lower, especially the estimated eruption time was ~50 min delayed as compared to the eruption onset calculated from the seismic and infrasonic data. This time shift can be explained by the late arrival of the CVID in the ionosphere. In addition, the errors in our method could be due to the approximations used: the spherical wave front of a CVID could be perturbed and slightly reshaped by horizontal atmospheric winds and the point source approximation might not work in the near field of volcano eruptions. Very likely, GNSS data with higher precision (such as 1 Hz GNSS measurements, as in the case of the studies the Tohoku-oki earthquake by *Astafyeva et al.* [2011, 2013b]) would show better results by using the same method. Otherwise, other approximations can be applied or different ionosphere-based methods could be developed in the future. Our work opens a new door in this direction.

Acknowledgments

This work is supported by the European Research Council under the European Union's Seventh Framework Program/ERC grant agreement 307998. We thank the SOPAC (<http://sopac.ucsd.edu>), UNAVCO (unavco.org), and RAMSAC (<http://www.ign.gob.ar>) online data services for the data of GNSS receivers. This is IPGP contribution 3791.

References

- Afraimovich, E. L., N. P. Perevalova, A. V. Plotnikov, and A. M. Uralov (2001), The shock-acoustic waves generated by the earthquakes, *Ann. Geophys.*, *19*(4), 395–409, doi:10.5194/angeo-19-395-2001.
- Afraimovich, E. L., E. I. Astafieva, and V. V. Kirushkin (2006), Localization of the source of ionospheric disturbance generated during an earthquake, *Int. J. Geomagn. Aeron.*, *6*, G12002, doi:10.1029/200403000092.
- Afraimovich, E., D. Feng, V. Kiryushkin, and E. Astafyeva (2010), Near-field TEC response to the main shock of the 2008 Wenchuan earthquake, *Earth Planets Space*, *62*(11), 899–904, doi:10.5047/eps.2009.07.002.
- Afraimovich, et al. (2013), A review of GPS/GLONASS studies of the ionospheric response to natural and anthropogenic processes and phenomena, *J. Space Weather Space Clim.*, *3*, A27, doi:10.1051/swsc/2013049.
- Astafyeva, E., K. Heki, V. Kiryushkin, E. Afraimovich, and S. Shalimov (2009), Two-mode long-distance propagation of coseismic ionosphere disturbances, *J. Geophys. Res.*, *114*, A10307, doi:10.1029/2008JA013853.
- Astafyeva, E., P. Lognonné, and L. Rolland (2011), First ionospheric images for the seismic slip on the example of the Tohoku-oki earthquake, *Geophys. Res. Lett.*, *38*, L22104, doi:10.1029/2011GL049623.
- Astafyeva, E., S. Shalimov, E. Olshanskaya, and P. Lognonné (2013a), Ionospheric response to earthquakes of different magnitudes: Larger quakes perturb the ionosphere stronger and longer, *Geophys. Res. Lett.*, *40*, 1675–1681, doi:10.1002/grl.50398.
- Astafyeva, E., L. Rolland, P. Lognonné, K. Khelifi, and T. Yahagi (2013b), Parameters of seismic source as deduced from 1 Hz ionospheric GPS data: Case study of the 2011 Tohoku-oki event, *J. Geophys. Res. Space Phys.*, *118*(9), 5942–5950, doi:10.1002/jgra.50556.
- Astafyeva, E., L. M. Rolland, and A. Sladen (2014), Strike-slip earthquakes can also be detected in the ionosphere, *Earth Planet. Sci. Lett.*, *405*, 180–193, doi:10.1016/j.epsl.2014.08.024.
- Billitz, D., L.-A. McKinnell, B. Reinisch, and T. Fuller-Rowell (2011), The international reference ionosphere today and in the future, *J. Geod.*, *85*, 909–920, doi:10.1007/s00190-010-0427-x.
- Blanc, E. (1985), Observations in the upper atmosphere of infrasonic waves from natural or artificial sources: A summary, *Ann. Geophys.*, *3*(6), 673–688.
- Cahyadi, M. N., and K. Heki (2015), Coseismic ionospheric disturbance of the large strike-slip earthquakes in North Sumatra in 2012: Mw dependence of the disturbance amplitudes, *Geophys. J. Int.*, *200*, 116–129, doi:10.1093/gji/ggu343.
- Calais, E., and J. B. Minster (1995), GPS detection of ionospheric perturbations following the January 17, 1994, Northridge earthquake, *Geophys. Res. Lett.*, *22*, 1045–1048, doi:10.1029/95GL00168.
- Calais, E., and J. B. Minster (1998), GPS, earthquakes, the ionosphere, and the space shuttle, *Phys. Earth Planet. Inter.*, *105*, 167–181, doi:10.1016/S0031-9201(97)00089-7.
- Caudron, C., B. Taisne, M. Garcés, L. P. Alexis, and P. Mialle (2015), On the use of remote infrasonic and seismic stations to constrain the eruptive sequence and intensity for the 2014 Kelud eruption, *Geophys. Res. Lett.*, *42*, 6614–6621, doi:10.1002/2015GL064885.
- Choosakul, N., A. Saito, T. Iyemori, and M. Hashizume (2009), Excitation of 4-min periodic ionospheric variations following the great Sumatra-Andaman earthquake in 2004, *J. Geophys. Res.*, *114*, A10313, doi:10.1029/2008JA013915.

- Coster, A., J. Williams, A. Weatherwax, W. Rideout, and D. Herne (2013), Accuracy of GPS total electron content: GPS receiver bias temperature dependence, *Radio Sci.*, *48*, 190–196, doi:10.1002/rds.20011.
- Dautermann, T., E. Calais, and G. S. Mattioli (2009a), Global Positioning System detection and energy estimation of the ionospheric wave caused by the 13 July 2003 explosion of the Soufrière Hills Volcano, Montserrat, *J. Geophys. Res.*, *114*, B02202, doi:10.1029/2008JB005722.
- Dautermann, T., E. Calais, P. Lognonné, and G. S. Mattioli (2009b), Lithosphere-atmosphere-ionosphere coupling after the 2003 explosive eruption of the Soufrière Hills Volcano, Montserrat, *Geophys. J. Int.*, *179*, 1537–1546, doi:10.1111/j.1365-246X.2009.04390.x.
- Galvan, D., A. Komjathy, M. P. Hickey, P. Stephens, J. Snively, Y. T. Song, M. D. Butala, and A. J. Mannucci (2012), Ionospheric signatures of Tohoku-Oki tsunami of March 11, 2011: Model comparisons near the epicenter, *Radio Sci.*, *47*, RS4003, doi:10.1029/2012RS005023.
- Heki, K. (2006), Explosion energy of the 2004 eruption of the Asama Volcano, central Japan, inferred from ionospheric disturbances, *Geophys. Res. Lett.*, *33*, L14303, doi:10.1029/2006GL026249.
- Heki, K., and J. Ping (2005), Directivity and apparent velocity of the coseismic ionospheric disturbances observed with a dense GPS array, *Earth Planet. Sci. Lett.*, *236*, 845–855, doi:10.1016/j.epsl.2005.06.010.
- Heki, K., Y. Otsuka, N. Choosakul, N. Hemmakorn, T. Komolmis, and T. Maruyama (2006), Detection of ruptures of Andaman fault segments in the 2004 great Sumatra earthquake with coseismic ionospheric disturbances, *J. Geophys. Res.*, *111*, B09313, doi:10.1029/2005JB004202.
- Hofmann-Wellenhof, B., H. Lichtenegger, and E. Wasle (2008) GNSS-Global Navigation Satellite Systems, *Springer*, doi:10.1007/978-3-211-73017-1.
- Kanamori, H., J. Mori, and D. G. Harkrider (1994), Excitation of atmospheric oscillations by volcanic eruptions, *J. Geophys. Res.*, *99*, 21,947–21,961, doi:10.1029/94JB01475.
- Kherani, E. A., P. Lognonné, H. Hebert, L. Rolland, E. Astafeyeva, G. Occhipinti, P. Coisson, D. Walwer, and E. R. Paula (2012), Modelling of the total electronic content and magnetic field anomalies generated by the 2011 Tohoku-oki tsunami and associated acoustic-gravity waves, *Geophys. J. Int.*, *191*(3), 1049–1066, doi:10.1111/j.1365-246X.2012.05617.x.
- Kiryushkin, V. V., and E. L. Afraimovich (2007), Determining the parameters of ionospheric perturbation caused by earthquakes using the quasi-optimum algorithm of spatiotemporal processing of TEC measurements, *Earth Planets Space*, *59*, 267–278, doi:10.1186/BF03353104.
- Kiryushkin, V. V., E. L. Afraimovich, and E. I. Astafeyeva (2011), The evolution of seismo-ionospheric disturbances according to the data of dense GPS network, *Cosmic Res.*, *49*(3), 227–239, doi:10.1134/S0010952511020043.
- Klobuchar, J. A. (1985), Ionospheric time delay effects on earth space propagation, in *Handbook of Geophysics and the Space Environment*, edited by A. S. Jursa chap. 10.8, pp. 1084–1088, U.S. Air Force, Washington, D. C.
- Komjathy, A., D. A. Galvan, P. Stephens, et al. (2012), Detecting ionospheric TEC perturbations caused by natural hazards using a global network of GPS receivers: The Tohoku case study, *Earth Planets Space*, *64*, 24, doi:10.5047/eps.2012.08.003.
- Liu, J. Y., Y. B. Tsai, S. W. Chen, S. P. Lee, Y. C. Chen, H. Y. Yen, W. Y. Chang, and C. Liu (2006), Giant ionospheric disturbances excited by the M9.3 Sumatra earthquake of 26 December 2004, *Geophys. Res. Lett.*, *33*, L02103, doi:10.1029/2005GL023963.
- Liu, J. Y., et al. (2010), Coseismic ionospheric disturbances triggered by the Chi-Chi earthquake, *J. Geophys. Res.*, *115*, A08303, doi:10.1029/2009JA014943.
- Liu, J. Y., C. H. Chen, C. H. Lin, H. F. Tsai, C. H. Chen, and M. Kamogawa (2011), Ionospheric disturbances triggered by the 11 March 2011 M9.0 Tohoku earthquake, *J. Geophys. Res.*, *116*, A06319, doi:10.1029/2011JA016761.
- Matoza, R., et al. (2011), Infrasonic observations of the June 09 Sarychev Peak eruption, Kuril Islands: Implications for infrasonic monitoring of remote explosive volcanism, *J. Volcanol. Geotherm. Res.*, *200*, 35–48, doi:10.1016/j.jvolgeores.2010.11.022.
- Nakashima, Y., K. Heki, A. Takeo, M. N. Cahyadi, A. Aditiya, and K. Yoshizawa (2016), Atmospheric resonant oscillations by the 2014 eruption of the Kelud volcano, Indonesia, observed with the ionospheric total electron contents and seismic signals, *Earth Planet. Sci. Lett.*, *434*, 112–116, doi:10.1016/j.epsl.2015.11.029.
- Occhipinti, G., L. Rolland, P. Lognonné, and S. Watada (2013), From Sumatra 2004 to Tohoku-oki 2011: The systematic GPS detection of the ionospheric signature induced by tsunamigenic earthquakes, *J. Geophys. Res. Space Phys.*, doi:10.1002/jgra.50322.
- Perevalova, N. P., V. A. Sankov, E. I. Astafeyeva, and A. S. Zhupityayeva (2014), Threshold magnitude for the ionospheric TEC response to earthquakes, *J. Atmos. Sol. Terr. Phys.*, *108*, 77–90, doi:10.1016/j.jastp.2013.12.014.
- Reddy, C. D., and G. K. Seemala (2015), Two mode ionospheric response and Rayleigh wave group velocity distribution reckoned from GPS measurement following Mw 7.8 Nepal earthquake on 25 April 2015, *J. Geophys. Res. Space Physics*, *120*, 7049–7059, doi:10.1002/2015JA021502.
- Rolland, L. M., G. Occhipinti, P. Lognonné, and A. Loevenbrück (2010), Ionospheric gravity waves detected offshore Hawaii after tsunamis, *Geophys. Res. Lett.*, *37*, L17101, doi:10.1029/2010GL044479.
- Rolland, L., P. Lognonné, E. Astafeyeva, A. Kherani, N. Kobayashi, M. Mann, and H. Munekane (2011), The resonant response of the ionosphere imaged after the 2011 Tohoku-oki earthquake, *Earth Planets Space*, *63*(7), doi:10.5047/eps.2011.06.020.
- Rolland, L. M., M. Vergnolle, J.-M. Nocquet, A. Sladen, J.-X. Dessa, F. Tavakoli, H. R. Nankali, and F. Cappa (2013), Discriminating the tectonic and non-tectonic contributions in the ionospheric signature of the 2011, Mw7.1, dip-slip Van earthquake, Eastern Turkey, *Geophys. Res. Lett.*, *40*, doi:10.1002/grl.50544.
- Watada, S., and H. Kanamori (2010), Acoustic resonant oscillations between the atmosphere and the solid earth during the 1991 Mt. Pinatubo eruption, *J. Geophys. Res.*, *115*, B12319, doi:10.1029/2010JB007747.

Erratum

In the originally published article, Figure 5 contained an error, which has since been corrected. Subsequently, it was noted that the supporting information was lacking two important animation files. These animation files are now present, and this version may be considered the authoritative version of record.